Available online at www.sciencedirect.com
ScienceDirect
Physics of the Earth and Planetary Interiors 166 (2008) 188–202
PHYSICS OF THE EARTH AND PLANETARY INTERIORS
www.elsevier.com/locate/pepi

Imaging laterally varying regional heterogeneities from seismic coda using a source-array analysis

Tae-Kyung Hong[a,*], William Menke[b]

[a] Yonsei University, Department of Earth System Sciences, Shinchon-dong, 134, Seodaemun-gu, Seoul 120-749, South Korea
[b] Lamont-Doherty Earth Observatory of Columbia University, 61 Route 9W, Palisades, NY 10964, USA

Received 7 March 2007; received in revised form 7 January 2008; accepted 13 January 2008

Abstract

Seismic coda is composed of scattered waves originated from various kinds of heterogeneities, whose locations are not confined in the great-circle ray-path direction between the source and receiver. We devise a technique to image laterally varying regional heterogeneities using single-station seismograms for clustered events. We analyze regional seismic records of the Borovoye seismic station for the Balapan nuclear explosions in Kazakhstan. Scattered waves that arrive coherently over the source arrays, are extracted by directional beamformings. The locations of scatterers responsible for the scattered waves are mapped from the beamforming direction, travel time and slowness (equivalently, phase velocity). The illuminated locations of heterogeneities are highly correlated with the structural variations in surface topography, crustal thickness and sedimentary thickness. The influence of the structural variations on seismic waves is quantified in terms of scattering intensity and quality factor. The scattering properties are observed to vary with phase due to the difference in frequency content and phase velocity. The proposed technique appears to be useful for a study of active tectonic regions with limited monitoring stations.

Keywords: Regional seismic wave; Quality factor; Scattering intensity; Laterally varying heterogeneity; Crustal heterogeneity

1. Introduction

Analysis of high-frequency waves is highly desired for a study of small-scale structures in the Earth. The resolution of imaged structures from a seismic inversion is normally dependent on the ray-path density and coverage. Thus, an imaging of small-scale structures with a conventional inverse technique requires an environment with the distribution of a high density of stations and events, which normally needs a long period of data collection. Such data acquisition, however, is not feasible in many regions with sparse monitoring system due to political and physical reasons, for instance, oceanic regions, politically restricted regions and aseismic regions. Regional seismic coda is a challenging record portion that may be useful for a study of such regions. Because the regional seismic coda is composed of high-frequency wavelets traveling in various crustal ray-paths that are not confined in the great-circle path between the source and receiver.

The seismic coda has, however, been rarely used for waveform or traveltime analysis since it is not possible to identify the wavelet with a certain ray path from a single coda section. Several approaches have been proposed to utilize scattered waves. One approach is a stochastic analysis of coda envelopes. The stochastic analysis does not require accurate knowledge on the ray-path trajectory of every scattered wave, and yields mean properties of the heterogeneities in the medium (e.g., Aki and Chouet, 1975; Hoshiba et al., 2001). This conventional analysis is most suitable for application to local areas (e.g., Chen and Long, 2000). Recently, this stochastic approach was extended to quantification of small-scale structures in the Earth's deep interior by analyzing precursors and coda of deep seismic phases with well-known ray paths (Hedlin et al., 1997; Vidale and Hedlin, 1998).

Several approaches to analyze the waveforms and traveltimes of scattered wavelets have been introduced. One attempt was to map the locations of heterogeneities near the sources from early

* Corresponding author. Tel.: +82 2 2123 2667; fax: +82 2 392 6527.
E-mail address: tkhong@yonsei.ac.kr (T.-K. Hong).

0031-9201/$ – see front matter © 2008 Elsevier B.V. All rights reserved.
doi:10.1016/j.pepi.2008.01.001

P-wave coda in regional or teleseismic array records for underground nuclear explosions (Boucher, 1973; Lay, 1987; Lynnes and Lay, 1989). Later, Revenaugh (1995) could image local heterogeneities at depths beneath station arrays by analyzing wavelets scattered from teleseismic waves that are recorded over the arrays. The strengths of scatterers were quantified in terms of stochastic parameters, such as semblance coefficient (e.g., Lay, 1987; Nikolaev and Troitskiy, 1987; Dainty and Schultz, 1995), scattering coefficient (e.g., Hoshiba et al., 2001) and quality factor (e.g., Mitchell, 1981).

In this study, we devise a technique to image laterally varying crustal heterogeneities from seismic coda of single-station records for events clustered. We quantify the strength of heterogeneity in terms of a net quality factor that combines the loss from intrinsic and scattering attenuation. We discuss the scattering features for the variations in known geological structures from the observed scattering intensity and quality factor.

2. Theoretical background: energy partition by scattering

During scattering, body waves accompany wavetype coupling (S-wave excitation by P-wave scattering, and vise versa) and surface waves have mode coupling. This wavetype and mode couplings cause partition of incident energy. The energy partition of body waves by scattering was widely studied (Frankel and Clayton, 1986; Shapiro et al., 2000; Hong and Kennett, 2003; Hong, 2004; Hong et al., 2005). Hereafter we call a scattered wavelet an 'in-phase' scattered wave when it has the same phase type as that of incident wave.

We examine the energy partition between in-phase and wavetype-coupled phases in the continental crust. The materials in the crust and lithosphere show high correlation between the seismic velocities and density (e.g., Birch, 1960; Stewart and Peselnick, 1977; Shiomi et al., 1997). Thus, the perturbations of seismic velocities and density in the crust and lithosphere can be expressed as (e.g., Sato and Fehler, 1998):

$$\xi(\mathbf{x}) = \frac{\delta\alpha(\mathbf{x})}{\alpha_0} = \frac{\delta\beta(\mathbf{x})}{\beta_0} = \frac{1}{K}\frac{\delta\rho(\mathbf{x})}{\rho_0}, \tag{1}$$

where $\xi(\mathbf{x})$ is the normalized velocity perturbation at a location of $\mathbf{x}$, and K is a constant to control the strength of density perturbation relative to the velocity perturbation. The parameters α_0 and β_0 are the background compressional and shear velocities, and ρ_0 is the background density. We consider three types of random media that include Gaussian, exponential and von Karman random media (e.g., Sato and Fehler, 1998; Hong and Kennett, 2003).

The mathematical expressions of in-phase and wavetype-coupled energy are given in Appendix A. We measure the energy ratio between in-phase and wavetype-coupled energy as a function of normalized wavenumber, ka. The energy ratio, R, is

$$R = \frac{\int_\phi \langle |u^{\mathrm{c}}(\phi)|^2\rangle \,\mathrm{d}\phi}{\int_\phi \langle |u^{\mathrm{i}}(\phi)|^2\rangle \,\mathrm{d}\phi}, \tag{2}$$

where ϕ is the scattering angle, $\langle |u^{\mathrm{i}}(\phi)|^2\rangle$ is the ensemble-averaged amplitude-square of in-phase scattered wave, and $\langle |u^{\mathrm{c}}(\phi)|^2\rangle$ is that of coupling-phase scattered wave (see Appendix A). The ensemble-averaged amplitude indicates the average wave amplitude from all possible forms of random media. We calculate the energy ratio for a crustal medium with the compressional-wave velocity (α_0) of 5.8 km/s and the shear-wave velocity (β_0) of 3.46 km/s. We set K in Eq. (1) to be 0.8 considering the seismic properties in the crust (Shiomi et al., 1997; Sato and Fehler, 1998).

For a case of shear-wave incidence, the energy ratio is observed to be lower than 0.04 over the entire ka range (Fig. 1). This observation indicates that in-phase scattering always prevails over wavetype-coupling scattering, regardless of the frequency of wave and the size of heterogeneity, when a shear wave is scattered. This theoretical expectation is consistent with previous observations for the composition of S coda (e.g., Aki, 1980; Fehler et al., 1992). In the case of compressional-wave incidence, wavetype-coupled scattered waves are stronger than in-phase scattered waves at low normalized wavenumbers (ka < 1), while in-phase scattering is dominant at high normalized wavenumbers (ka > 1). This observation suggests that low-frequency P-waves are scattered much into S-waves. Thus, for instance, when a P-wave with a dominant frequency of 2 Hz propagates through a heterogeneous medium with a correla-

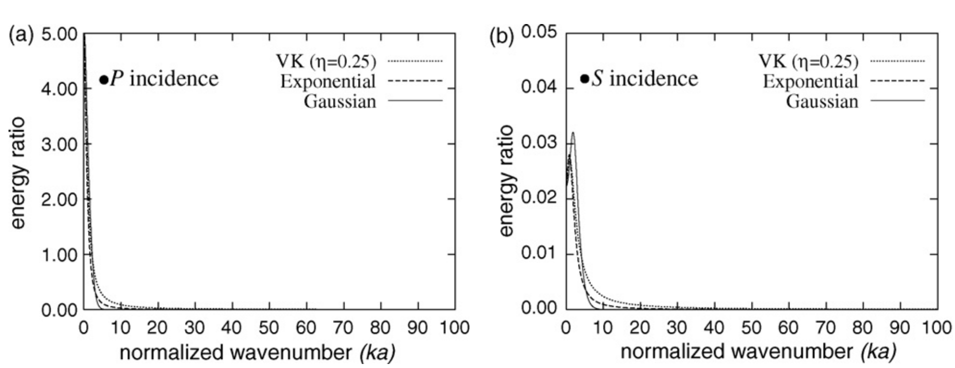

Fig. 1. Energy ratios, R, between in-phase and wavetype-coupled scattered waves in elastic random media (von Karman, exponential, Gaussian). (a) Scattered energy ratios for P-wave incidence case (R = [PS energy]/[PP energy]) and (b) for S-wave incidence case (R = [SP energy]/[SS energy]). In the P-wave incidence case, the wavetype-coupled scattered waves are stronger than in-phase scattered waves at low normalized wavenumbers, ka < 2. In-phase scattered waves are dominant over wavetype-coupled scattered waves in the entire ka range for the S-wave incidence case.

tion distance of 9 km or smaller, the scattered wavefield will be dominated by S-waves.

Like a wavetype coupling in body-wave scattering, surface waves accompany mode coupling during scattering. The radiation patterns of mode-coupled scattered waves are well understood (e.g., Snieder, 1986; Bostock, 1991). The radiation pattern changes with the mode coupled, but a stochastic balance between earned and lost energy is established in a series of mode couplings (Snieder, 1988). Thus, the energy scattered from surface wave can be regarded to be radiated isotropically in a stochastic sense (Snieder, 1988; Sato and Nishino, 2002).

The regional scattered waves that we analyze in this study travel in far-regional distances. Thus, they possess strong impetus of lateral propagation along the crust or mantle lid. Lateral heterogeneities that extend vertically are most effective scatterers for such laterally propagating waves. Seismic waves are scattered with a vertical takeoff angle close to the vertical incidence angle for such lateral heterogeneities. Thus, stochastically, the scattered waves share the horizontal slowness of the incident wave. In this study, we analyze shear phases (Sn, Lg, Rg), which are rarely wavetype-coupled during scattering, unlike P phases. Thus, a scattering of shear wave or surface wave can be regarded as an in-phase scattering process.

3. Data and geology

We use regional seismic records of the Borovoye station (BRV) for underground nuclear explosions (UNEs) at the Balapan test site, Kazakhstan during 1968–1989 (Fig. 2). The recording system of BRV is composed of a set of short-period vertical instruments (Kim et al., 2001; Hong and Xie, 2005). The sensor type of the seismometers is SKM-3 with a natural period of 2.0 s and sampling rates of 0.032 and 0.096 s. The nominal sensitivities (gains) of the seismometers are 20, 200, 1000 and 2000 counts/μm (Kim et al., 2001). Since coda waves attenuate exponentially with time, we use both low-gain (20 and 200 counts/μm) and high-gain (1000 and 2000 counts/μm) seismograms to minimize digital round-off error. High-gain records are used for the analysis at the lapse times of 400–900 s. The numbers of low- and high-gain records are 46 and 35, respectively (Fig. 2). The records display a high signal-to-noise ratio (Fig. 3).

The body-wave magnitudes, m_b, of the UNEs are 4.8–6.2. The distances between BRV and UNEs are around 690 km. High-precision locations and origin times are available from various sources (NNCRK, 1999; Thurber et al., 2001; Kim et al., 2001). The aperture of the source array is around 19 km in the longitudinal direction (Fig. 2). The average depth of burial is 465 m below the surface, and the mean depth deviation is 73 m. The average horizontal spacing between adjacent events is 1.42 km.

The shear velocities in the mantle lid of Kazakhstan reach 4.7 km/s (Quin and Thurber, 1992). The crustal thickness (CRUST2.0, Bassin et al., 2000), sedimentary layer thickness (Laske and Masters, 1997), surface topography (GTOPO30, compiled by the U.S. Geological Survey), and major geological setting (e.g., Levashova et al., 2003) are shown in Fig. 4. The

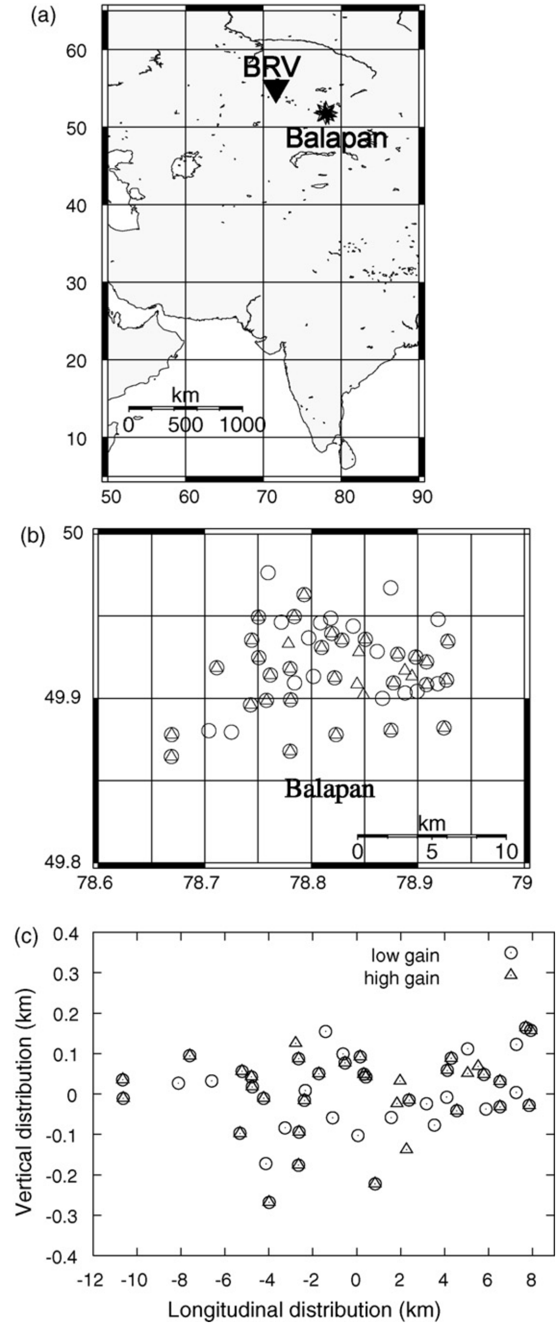

Fig. 2. Map and event locations. (a) Map of the Borovoye seismic station (BRV) and the Balapan test site, Kazakhstan (Balapan). (b) Underground nuclear explosions at the Balapan test site. The numbers of events recorded at low-gain and high-gain seismometers are 46 and 35, respectively. Most events were recorded at both low- and high-gain seismometers. (c) Vertical variation of events relative to the reference location of 49.92°N and 78.82°E, and 155 m below the sea level, in a view on the longitudinal direction. The vertical deviation from the average depth varies up to 300 m. The source-array aperture is about 19 km in the longitudinal direction.

study area is a complex of 4 tectonic blocks (Fig. 4(d)); block A is the West Siberian Basin, block B is the European Craton, block C is the Tarim Basin, and block E is the Turan Plate. The hard rock area, block D, in which the Balapan test site and the Borovoye Observatory are placed is composed of precambrian and early palaeozoic rocks (Levashova et al., 2003). The sedi-

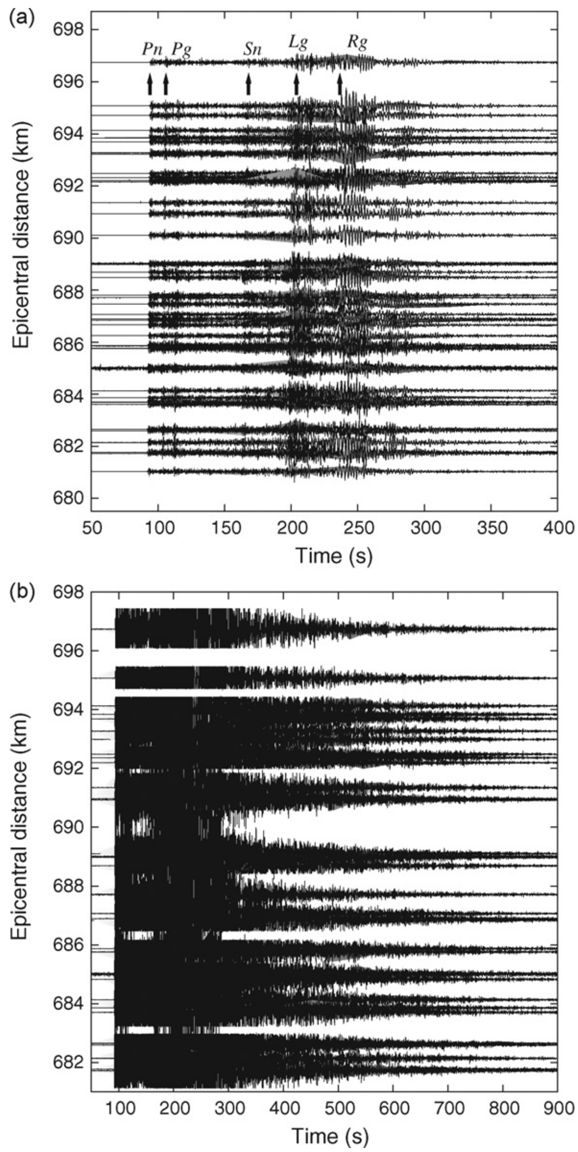

Fig. 3. Vertical-component displacement seismograms used for the study: (a) 46 low-gain records and (b) 35 high-gain records. The coda amplitudes of low-gain seismograms are very low at long lapse times, and are subject to digitizing round-off error. The high-gain records are used for the analyses with lapse times after 400 s.

mentary regions in Fig. 4(b) correspond to the basins and cratons in Fig. 4(d).

4. Method: beamforming of source-array records and positioning of scatterer

In this section, we present a methodology to process source-array records. We also describe the scheme to determine the location of scatterer. After the beamforming of source-array records, we perform further analyses for assessment of isochronous scattering power or quality factor, which are described in the following sections (Sections 5 and 7).

Under the spatial reciprocity theorem (Aki and Richards, 1980), single-station records for clustered events can be regarded as fictitious receiver-array records in the reciprocal geometry. Source-array analyses have been used for studies of phase composition in the nearfield and seismic properties in the source region (Spudich and Bostwick, 1987; Gupta et al., 1990; Scherbaum et al., 1991; Xie et al., 1996; Hong and Xie, 2005).

Coherent energy arriving over an array can be extracted using a slant-stacking (Kanasewich, 1981; Matsumoto et al., 1998; Rost and Thomas, 2002). The incoming direction of the coherent energy can be controlled with the beamforming direction in slant-stacking. The phase in interest can be controlled with the slowness in slant-stacking. As we analyze source-array records, we can identify the original phase velocity before scattering from scattered wavefield. In other words, we can classify the scattered wavelets in terms of their original phase velocities.

The beamforming is made for all azimuthal angles, θ, from 0 to 2π. Incoherent scattered waves are suppressed during slant-stacking. Multi-scattered waves that are included in a slant-stacked record should be much weaker than single-scattered waves in the same time-window because multi-scattered waves are attenuated further than single-scattered waves due to multiple energy partitioning. Thus, we can assume that the coherent energy in the slant-stacked coda is dominantly composed of single-scattered energy. As shear wave is dominantly scattered into the same-phase energy (Section 2), slant-stacked records of seismic coda are mainly composed of in-phase single-scattered wavelets.

The slant-stacked record, $u_s^j(t)$, of source-array records for a beamforming direction of θ_j is calculated by

$$u_s^j(t) = \frac{1}{M}\sum_{i=1}^{M} u_i(t - \Delta r_i^j \cdot s_h), \tag{3}$$

where u_i is the seismogram of the ith event, M is the number of total events, and s_h is the horizontal slowness. The relative distance, Δr_i^j, is given by

$$\Delta r_i^j = r_i^j - r_0, \tag{4}$$

where r_i^j is the distance between the location of event, $\mathbf{x}_i$, and an imaginary location of $\mathbf{y}_j$ in the direction of beamforming, θ_j. The reference radius, r_0, is the average distance between the station and sources (Fig. 5). The imaginary reference location ($\mathbf{y}_j$) is given by

$$\mathbf{y}_j = \mathbf{x}_0 + (r_0 \sin\theta_j, r_0 \cos\theta_j), \tag{5}$$

where $\mathbf{x}_0$ is the central location of the sources. Here, the reference radius, r_0, should be sufficiently larger than both the relative distance Δr_i^j and array aperture, L_{ap} (i.e., $r_0 \gg \Delta r_i^j$, $r_0 \gg L_{ap}$) so that the waves incident to the array can be approximated to be plane waves.

From Fig. 5, the apparent distance r_i^j changes with the beamforming direction (θ_j), which causes successively a change in the order of records as function of distance (see also Fig. 6). The phase velocity (horizontal slowness), an input parameter for slant-stacking, naturally controls the phase and depth of imaging. Since the phase velocity of coherent scattered wavelet is a known parameter, the traveltime of wave can be directly inverted to travel distance. Thus, we can determine the loca-

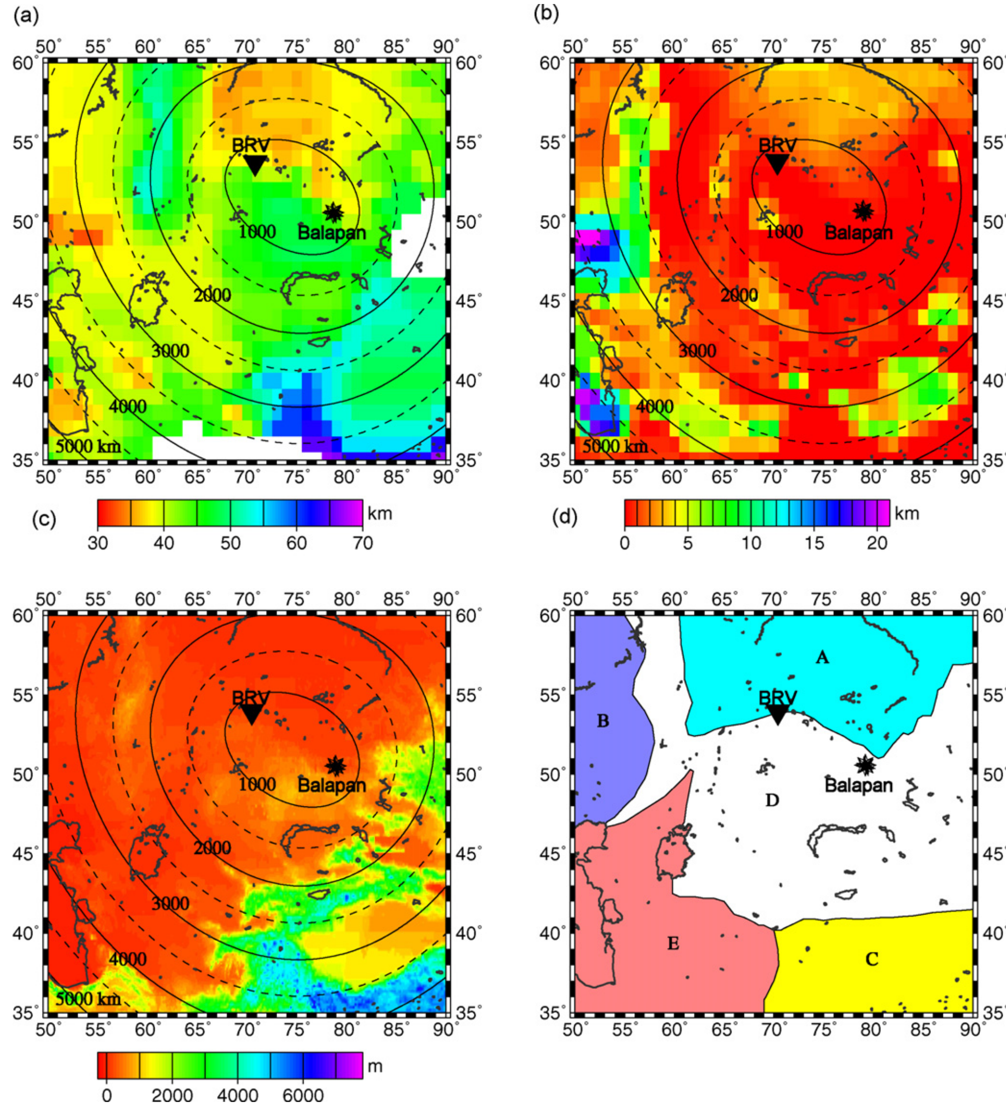

Fig. 4. Major crustal and geological structures in the central Asia. (a) Crustal thickness (CRUST2.0), (b) sedimentary thickness, (c) surface topography (GTOPO30), and (d) major geological structures (modified after Levashova et al., 2003). Iso-travel distances are marked with lines in every 500 km. The locations of receiver and source array correspond to the two foci of iso-travel distance ellipses.

tion of scatterer from the wave direction (θ_j) and travel distance (Fig. 7).

The locations of scatterers are determined in the single-scattering concept, which satisfies the fractional energy loss by energy partitioning on the interfaces of heterogeneities. When an elastic wave is incident to a mildly perturbed medium, fractional energy is back-scattered while the primary energy keeps propagating in the forward direction (Aki and Richards, 1980; Wu, 1982; Hong and Kennett, 2003). Thus, the primary energy propagates until it is totally dissipated. This concept may not be applicable for some extreme cases where seismic waves are extincted abruptly, such as the Lg crossing the oceanic crust (e.g., Zhang and Lay, 1995; Kennett and Furumura, 2001).

We analyze three regional phases, Rg, Lg and Sn waves in this study. Here, Rg is the fundamental-mode Rayleigh wave of which amplitude decreases exponentially with depth. The Rg is sensitive to most structural variations in the crust. The Lg is a set of crustally guided shear waves with typical group velocities of 3.0–3.6 km/s (e.g., Kennett, 2002). This Lg wave can be also described as a higher mode Rayleigh wave in a mode theory. This Lg phase is not only sensitive to shallow crustal structures, but also to lower crustal structures. The Sn wave is the mantle-refracted shear wave that travels through the mantle lid. The Sn is sensitive to structural variations around the Moho.

We implement a phase velocity of 3.0 km/s for analysis of Rg, 4.2 km/s for analysis of Lg and 4.8 km/s for analysis of Sn, following the recent studies on the phase composition of Balapan UNE records (Hong and Xie, 2005; Hong and Menke, 2008). The source-array records are bandpass filtered before slant-stacking. We apply a bandpass filtering range of 0.2–0.8 Hz for Rg, 0.5–2.0 Hz for Lg and 0.5–3.0 Hz for Sn, considering the frequency contents of the regional phases (Hong and Xie, 2005). The phase velocities of Lg and Rg are determined constant in the frequency ranges (Hong and Xie, 2005). Thus, the Lg and Rg can be analyzed as non-dispersive waves in the given frequency ranges.

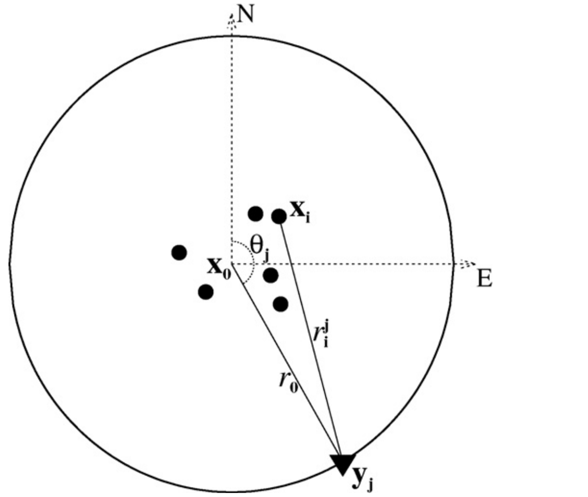

Fig. 5. Schematic diagram of source-array beamforming for an azimuthal angle of θ_j. The source array (clustered events) is marked with solid circles, and an imaginary reference location for beamforming direction is marked with an inverted triangle. The reference location of the source array is $\mathbf{x}_0$, the location of ith event is $\mathbf{x}_i$, and the location of an imaginary receiver is $\mathbf{y}_j$. The distance between $\mathbf{y}_j$ and $\mathbf{x}_0$ is r_0 which is constant for a change in azimuthal angle. The distance between $\mathbf{y}_j$ and $\mathbf{x}_i$ is r_i^j.

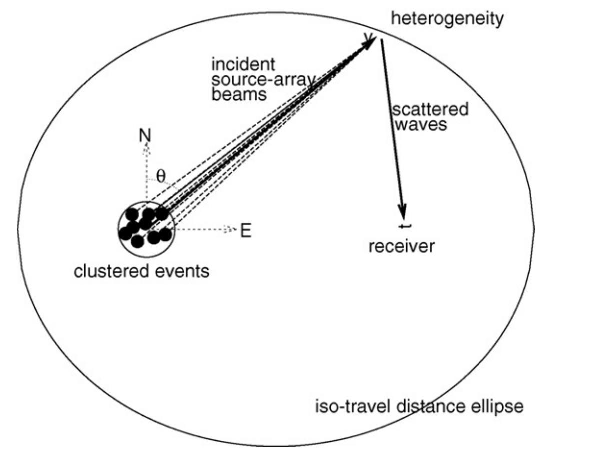

Fig. 7. Schematic diagram for positioning of a heterogeneity from the traveltime, beamforming direction and phase velocity. Source-array beams that are radiated into an azimuthal direction of θ are back-scattered by a heterogeneity, and the scattered waves are recorded at a receiver. The locations of events and receiver are the foci of iso-travel distance ellipses. The size of iso-travel ellipse is determined by the traveltime and phase velocity. Coherent scattered waves with a common phase velocity can be assessed by slant-stacking the source-array records.

5. Result: isochronous scattering power

The scattering intensity is proportional to the fractional energy loss. We quantify the scattered energy in a time-window of a slant-stacked record. The average amplitude-squares, w_s^θ, at a time-window can be calculated by

$$w_s^{\theta_j}(t_n) = \frac{1}{N}\sum_{k=1}^{N}|u_s^j(t_{n-N/2+k})|^2, \tag{6}$$

where θ_j is the jth azimuthal angle (beamforming direction), t_n is the nth discrete time, u_s^j is the slant-stacked record for an azimuthal angle of θ_j in Eq. (3), and N is the total number of discrete sampling times of the time-window. The time-window sizes applied for this analysis are 30 s for Rg, 20 s for for Lg, and 14 s for Sn.

To illuminate scatterers in the medium under a uniform intensity scale, we normalize the scattering intensity $w_s^{\theta_j}(t_n)$:

$$P_s(\theta_j, t_n) = \frac{w_s^{\theta_j}(t_n)}{w_{\max}(t_n)}, \tag{7}$$

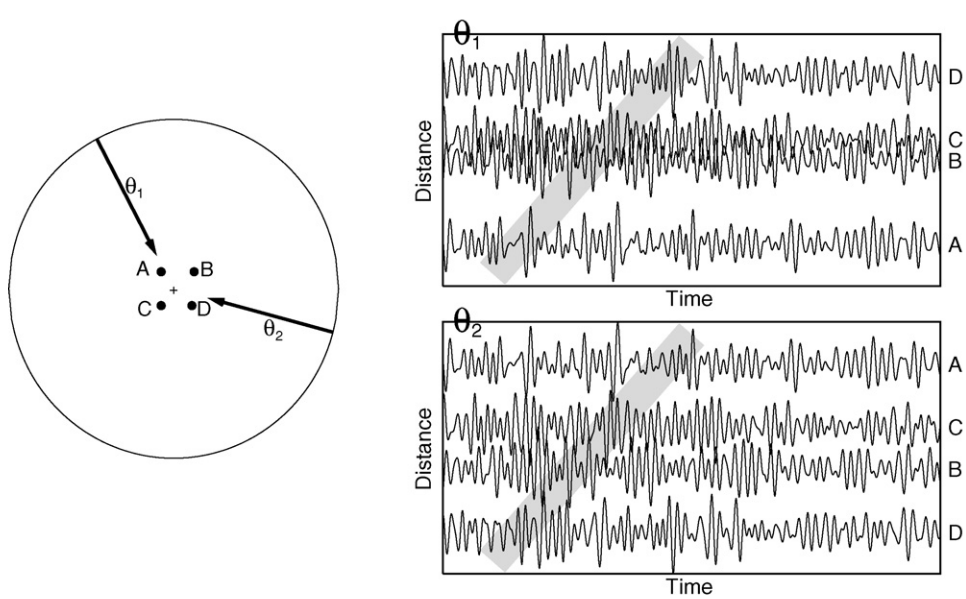

Fig. 6. An example of slant-stacking with four-component array records for two different beamforming directions, θ_1 and θ_2. The time is arbitrary in this example. The distance between array and imaginary reference location changes with a beamforming direction, which causes a change in the order of records for distance. The shaded areas indicate the wavelets that are stacked.

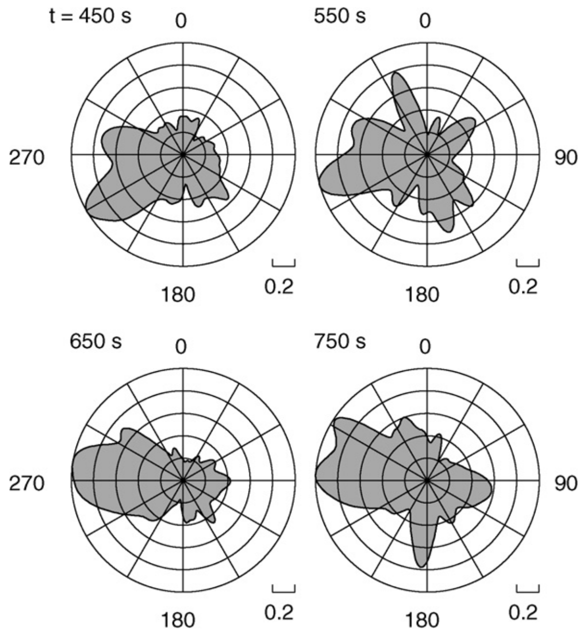

Fig. 8. Variation of normalized scattered Lg energy variation with azimuthal angle at various lapse times ($t = 450, 550, 650, 750$ s). The scattered energy is normalized for the maximum strength. The normalized magnitude represents the relative strength of scattered energy over azimuthal angles at a given time.

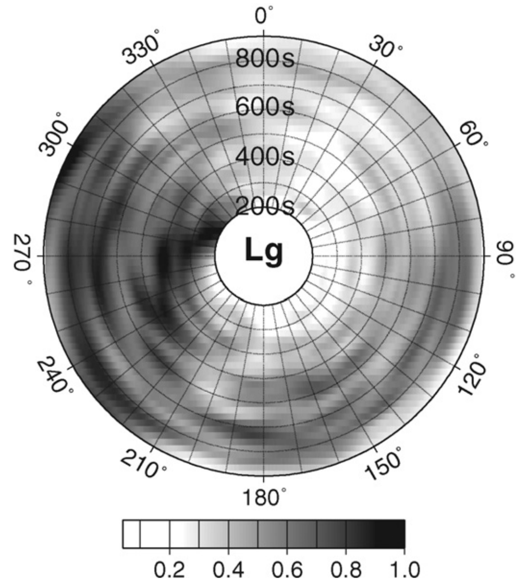

Fig. 9. An integrated result of temporal normalized Lg scattering energy shown in Fig. 8. The color indicates the normalized scattering intensity that corresponds to the amplitude in the rose diagram of Fig. 8. The lapse times and the azimuthal angles are annotated. The temporal variation can be converted to a spatial variation of scattering intensity using a backprojection scheme.

where the normalization factor $w_{\max}(t_n)$ is the maximum scattering intensity on the isochrone:

$$w_{\max}(t_n) = \max[w_s^{\theta_j}(t = t_n), \quad j = 1, 2, \ldots, J]. \tag{8}$$

Here, J is the number of total discrete azimuthal angles. An example of normalized intensity of Lg-origin scattered energy estimated from the source-array coda is presented in Fig. 8. The normalized scattering intensity results for all discrete times are integrated to produce a combined result (Fig. 9). This temporal variation of scattering intensity is converted to a spatial distribution of scatterers using the scatterer positioning scheme described in Section 4 (Fig. 10).

The observed scattering intensity appears to be consistent among various phases (Fig. 10). The illuminated scatterer locations agree with the geological structures in Fig. 4. The seismic scattering on geological and tectonic structures has been widely observed (Zhang and Lay, 1994; Dainty and Schultz, 1995; La Rocca et al., 2001). The ray path changes with the phase and scattering strength is dependent on the frequency content. Thus, the influence of a geological structure on scattering changes with the phase and frequency.

6. Verification test

6.1. Correlation with geological structures

We check the correlation between scattering intensity and geological structures for a verification of the technique before we proceed further to assessment of quality factor. The vertical variations of geological structures are normalized for the correlation measurement. To examine the correlation between scattering intensity and vertical variation of geological structure in a local area, we measure two local-correlation quantities (C_1, C_2):

$$C_1(\mathbf{x}) = P_s(\mathbf{x}) \cdot \frac{\delta G_{\mathbf{x}}}{\delta G_{\max}}, \qquad C_2(\mathbf{x}) = \frac{1}{2}\left(P_s(\mathbf{x}) + \frac{\delta G_{\mathbf{x}}}{\delta G_{\max}}\right), \quad \mathbf{x} \in \mathbf{A}, \tag{9}$$

where $P_s(\mathbf{x})$ is the normalized scattering intensity at location $\mathbf{x}$, $\delta G_{\mathbf{x}}$ is the vertical variation of geological structure at location $\mathbf{x}$, and $\delta G_{\max}$ is the maximum variation in the study area ($\mathbf{A}$):

$$\delta G_{\mathbf{x}} = |G_{\mathbf{x}} - G_0|, \qquad \delta G_{\max} = \max[\delta G_{\mathbf{x}}, \ \mathbf{x} \in \mathbf{A}]. \tag{10}$$

Here $G_{\mathbf{x}}$ is the vertical scale of geological structure at location $\mathbf{x}$, and G_0 is the average value of $G_{\mathbf{x}}$ along the great-circle path between the sources and the receiver.

As the scattering coefficients and vertical variations are normalized, their local-correlation quantities (C_1, C_2) are determined between 0 and 1. Both local-correlation quantities give values close to 1 for high correlation (Fig. 11). In particular, local-correlation quantity C_1 suppresses uncorrelated feature highly, and displays the correlated feature well. Since scattering intensity is proportional to the magnitude of structural variation, a high local-correlation quantity is expected in the region with a large structural variation. When scattered energy is rarely excited by a structural variation, the local-correlation quantity should be estimated low.

From the local correlation test, we can verify the methodology. Also, we can quantify the relative influence of each structural variation on scattering. In Fig. 11, we present the local-correlation quantities between the Lg scattering intensity and geological structures. It is clearly shown that the determined scatterer locations are highly correlated with the variations in sedimentary thickness, crustal thickness and surface topogra-

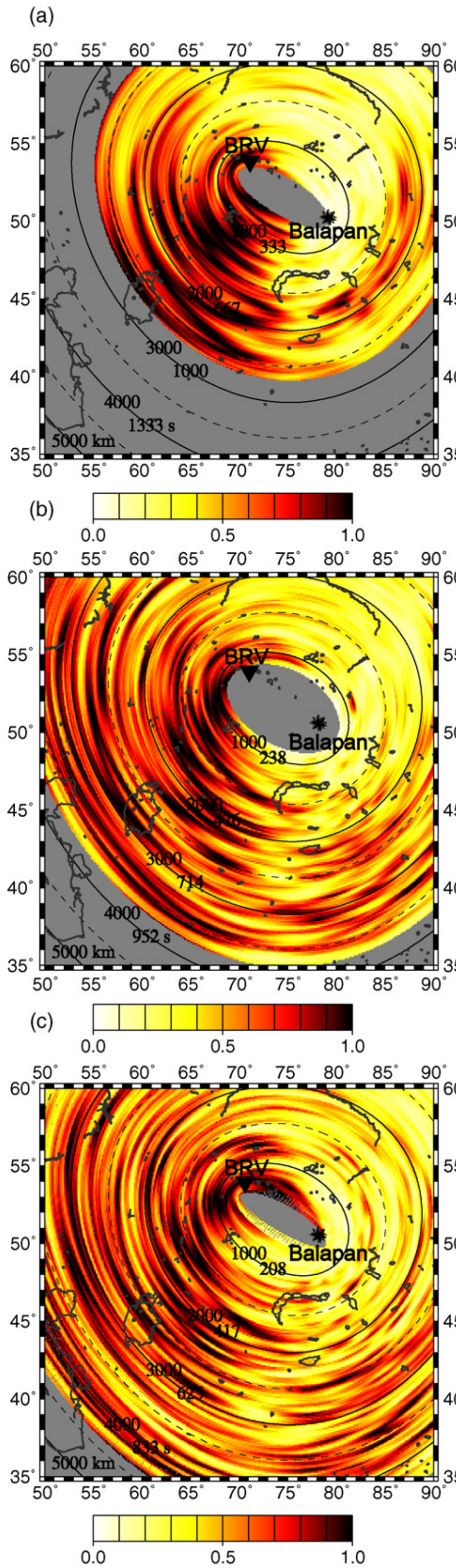

Fig. 10. Spatial variations of normalized scattering intensities, estimated from (a) Rg, (b) Lg and (c) Sn scattered waves. Iso-travel distance lines are presented. The illuminated scattering locations agree well with the geological structures in Fig. 4.

phy. We thus confirm that the proposed technique resolves well the structural variations in the crust. In the following section, we proceed to quantify the influence of structural variation in terms of quality factor, Q.

6.2. Bootstrapping and random-shuffling test

In the previous section, we have shown that the observed feature is remarkably correlated with the geological structures. We now examine whether the observed features are artifacts by the influence of factors other than scattering, such as interference of other events and inherent influence of array geometry. The source-array analysis is based on records for events at different times. Thus, the energy from incoherent temporary sources, e.g., natural earthquakes, is well suppressed in the analysis. This characteristic of source-array analysis allows us to interpret the source-array data with reduction of artifacts by contemporary earthquakes.

The geometry of array may be another possible source to cause artifacts in the array analysis. The source arrays of this study spread in a region of 19 km $\times$ 13 km, and are densely populated (Fig. 2(b)). The influence of array geometry can be examined with random-shuffling test; array analyses are preformed for randomly shuffled records under the same array geometry. This test allows us to examine the presence of any consistent artifacts caused by the array geometry. We constitute 32 randomly shuffled sets for the test.

The scattering intensity from a randomly shuffled set illustrates random distribution of small-scale scatterers over the region, which is apparently different from the result of the original data set (Fig. 12(a) and (b)). The distribution of scattering intensity varies by the random set, and any coherent feature is not observed among the 32 randomly shuffled sets. As a result, the average scattering intensity of the 32 sets is shown to be plain without any noticeable variation (Fig. 12(c)). The average scattering intensities of the 32 sets are estimated by 0.43–0.71 over the region, and its standard deviations are given by 0.08–0.25 (Fig. 12(c) and (d)). Thus, we confirm that the original results from source-array analysis are not affected by the array geometry.

We also examine the consistency and stability of the results using the bootstrap method (Efron and Tibshirani, 1991; Revenaugh and Meyer, 1997; Lay et al., 2004). We constitute 32 bootstrap sets. The number of bootstrap sets, 32, is large enough for reliable statistical analysis (Efron and Tibshirani, 1991). Each bootstrap set is constituted by data that are randomly selected from the original data set, with allowance of multiple selection. The bootstrap analysis allows us to examine the reliability of the original result based on the full data set.

We perform the scattering-intensity analysis for the 32 bootstrap sets. We find that the results from each bootstrap analysis are consistent, and are fairly close to the original analysis results (Fig. 13(a)–(c)). The standard deviations among the 32 bootstrap analysis are estimated by 0.001–0.17. Here note that the standard deviations from the bootstrap analysis are far lower than those from the random-shuffling test, which supports the appearance of consistent patterns among the 32 sets. From the

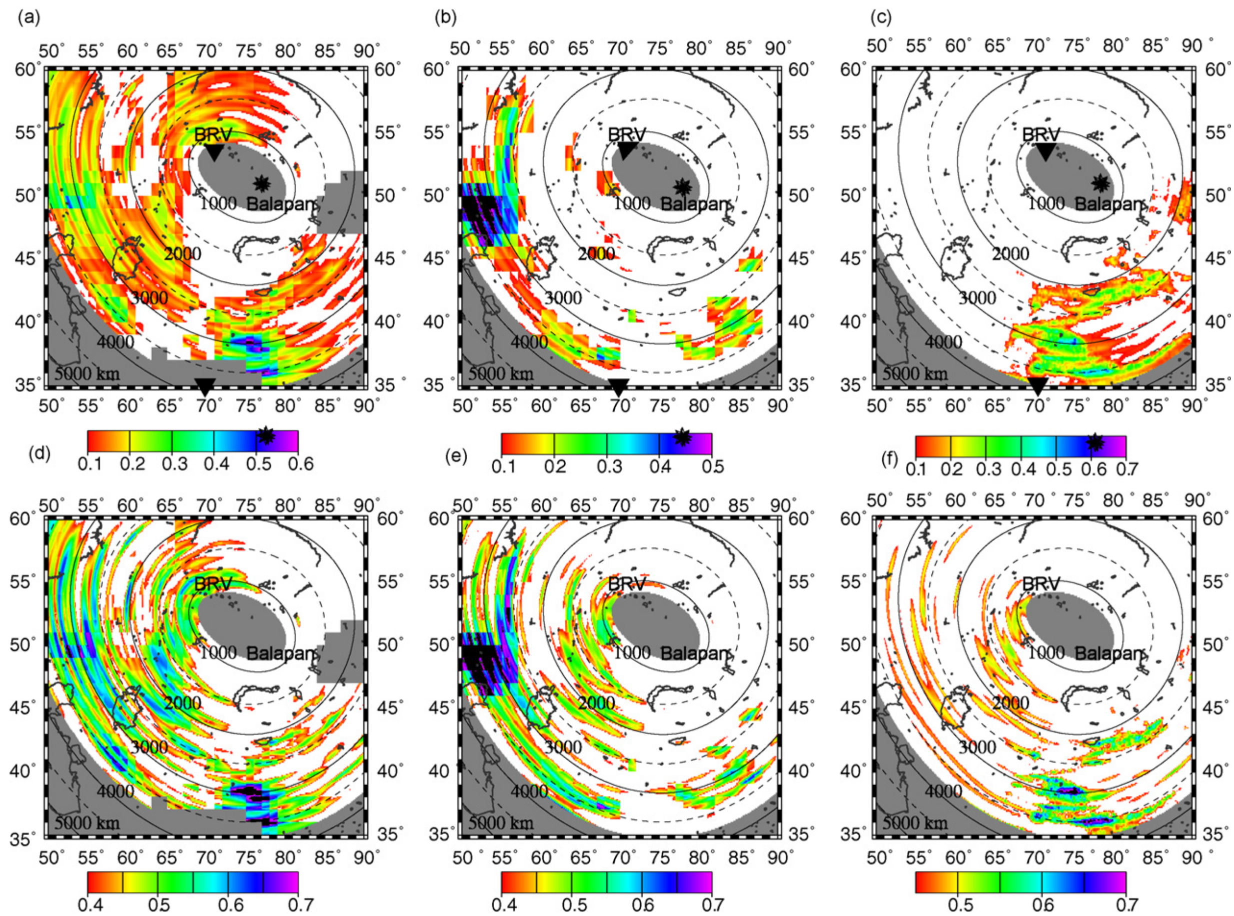

Fig. 11. Examination of local correlation between observed Lg scattering intensity and geological structure. The local-correlation quantities are calculated from Eq. (9). The upper figures are C_1 variations for (a) crustal thickness, (b) sedimentary thickness and (c) surface topography. The lower figures (d–f) are C_2 variations for the same geological structures. Both tests display high correlation with geological structures.

random-shuffling and bootstrapping tests, we confirm that the results from the source-array analysis are pure observations.

7. Result: quality factor, *Q*

We quantify the strength of scatterer in terms of apparent quality factor, Q. The temporal decay of coda can be expressed by (Toksöz et al., 1988; Sato and Fehler, 1998)

$$A(t) = A_0 \frac{1}{t^p} \exp\left[-\frac{\omega t}{2Q_c}\right], \tag{11}$$

where ω is the angular frequency, t is a lapse time, A_0 is a constant for the initial level of coda, Q_c is the coda Q, and p is the geometrical spreading parameter: $p = 1.0$ for body waves, $p = 0.75$ for diffuse waves, and 0.5 for surface waves.

We first measure the representative Q_c from the coda at lapse times after 500 s where scattered wavefields are expected mixed well. The lapse time of 500 s corresponds to 3 times the Sn traveltime, 2.5 times the Lg traveltime, and twice the Rg traveltime. We apply a geometrical spreading parameter of 0.5 for analyses of Rg and Lg scattered waves, and 1.0 for an analysis of Sn scattered waves. The mean Q_c is estimated by 361 ± 29 for Rg at frequencies of 0.2–0.8 Hz, 742 ± 36 for Lg at frequencies of 0.5–2.0 Hz, and 1201 ± 66 for Sn at frequencies of 0.5–3.0 Hz.

When an incident wave is scattered by a heterogeneity, the total first-order scattered energy with travel time t can be expressed as the sum of directional scattered energy:

$$\Delta E_T(t) = \int_0^{2\pi} \Delta E(\theta, t)\, d\theta, \tag{12}$$

where $\Delta E(\theta, t)$ is the scattered energy in the direction of θ and the travel time of t. Thus, the average angular scattered energy is then given by

$$\langle \Delta E \rangle(t) = \frac{1}{2\pi} \Delta E_T(t) = \frac{1}{J} \sum_{j=1}^{J} \Delta E(\theta_j, t), \tag{13}$$

where J is the number of discrete azimuthal angles, and $\langle \Delta E \rangle(t)$ is the mean scattered energy at travel time t.

The energy is proportional to the square of wave amplitude. From Eq. (11), the square of coda amplitude, $w(t)$, can be written by

$$w(t) = w_0 \frac{1}{t^{2p}} \exp\left[-\frac{\omega t}{Q_c}\right], \tag{14}$$

where w_0 is a constant. The temporal decay rate of coda in slant-stacked record is the same with that of single-station records

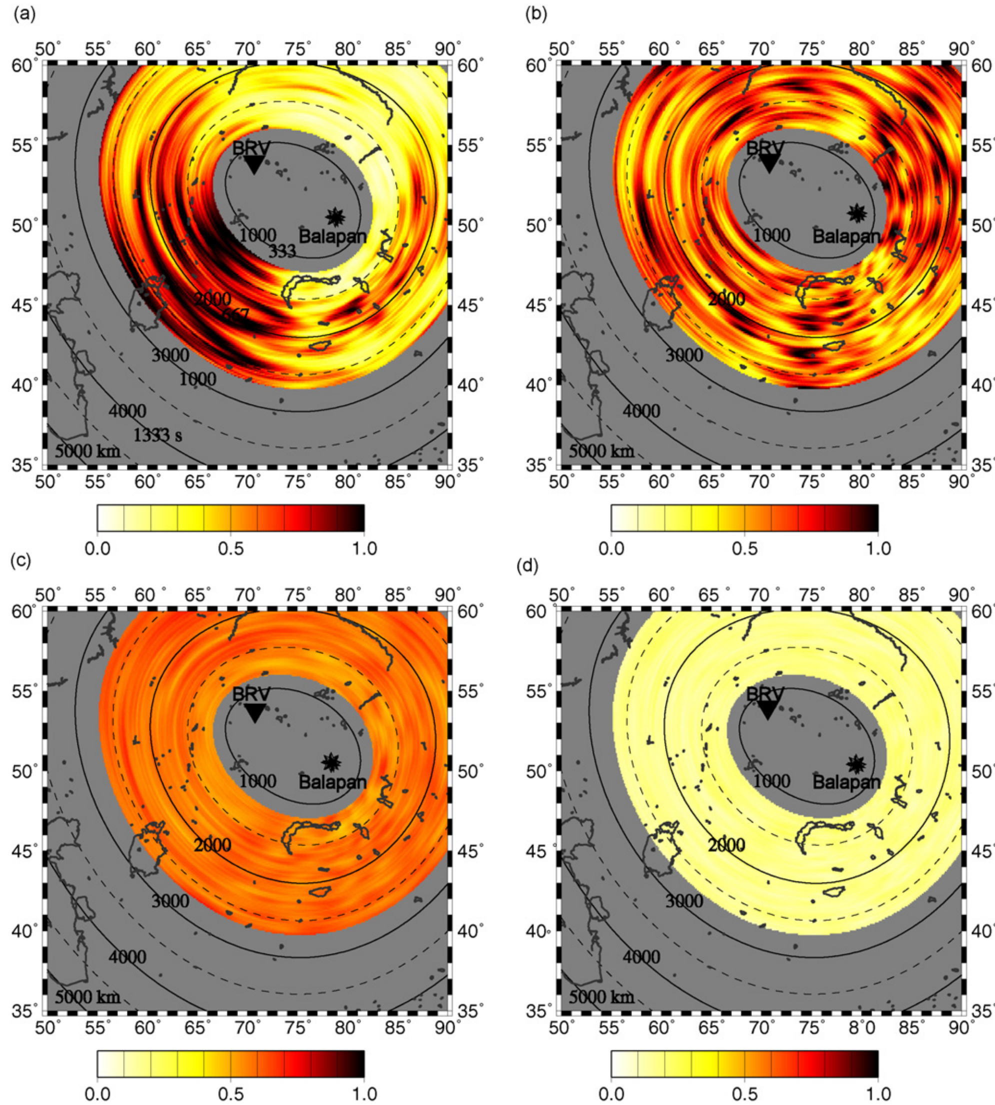

Fig. 12. Random-shuffling test of Rg scattering intensity: (a) the Rg scattering intensity from the original data set, (b) an estimate of Rg scattering intensity for a random-shuffling set, (c) the average of the results from the 32 random-shuffling sets, and (d) the standard deviation among the 32 estimates. The estimate from a random set displays a pattern that is fairly different from the original result. The estimate varies by random set, and does not show any coherent feature. Thus, the average of the estimates from the random sets is observed to be plain.

(e.g., Matsumoto et al., 2001). Thus, we can construct the reference slant-stacked coda envelope similarly:

$$w_{\mathrm{s}}^{\theta}(t) = w_0^{\theta}\,\frac{1}{t^{2p}}\,\exp\left[-\frac{\omega t}{Q_{\mathrm{c}}}\right], \quad (15)$$

where $w_{\mathrm{s}}^{\theta}(t)$ is the square of amplitude of slant-stacked coda for the beamforming direction of θ, and the reference square of amplitude w_0^{θ} varies with the beamforming direction. The employment of the direction-dependent reference coda level (w_0^{θ}) reflects not only the influence of anisotropic scattering on the boundaries of heterogeneities, but also the inherent interaction with the medium along ray path.

We now proceed to derive an equation for determination of Q from the coda envelopes. The seismic quality factor is inversely proportional to the energy loss (Wu, 1982):

$$Q^{-1}(k) = \frac{1}{Vk}\,\frac{\Delta E}{E}, \quad (16)$$

where k is the wavenumber, and V is the volume of heterogeneous medium through which the incident wave passes. Thus, the reference quality factor, Q_{ref}, can be determined by

$$Q_{\mathrm{ref}}^{-1}(k) = \frac{1}{Vk}\,\frac{\Delta E_{\mathrm{ref}}}{E}, \quad (17)$$

where ΔE_{ref} is the mean coda envelope of slant-stacked record. The level of coda temporally increases from the reference coda envelope when more scattered energy arrives due to influence of localized heterogeneities. On the other hand, the level of coda decreases when the scattering is less active than the average.

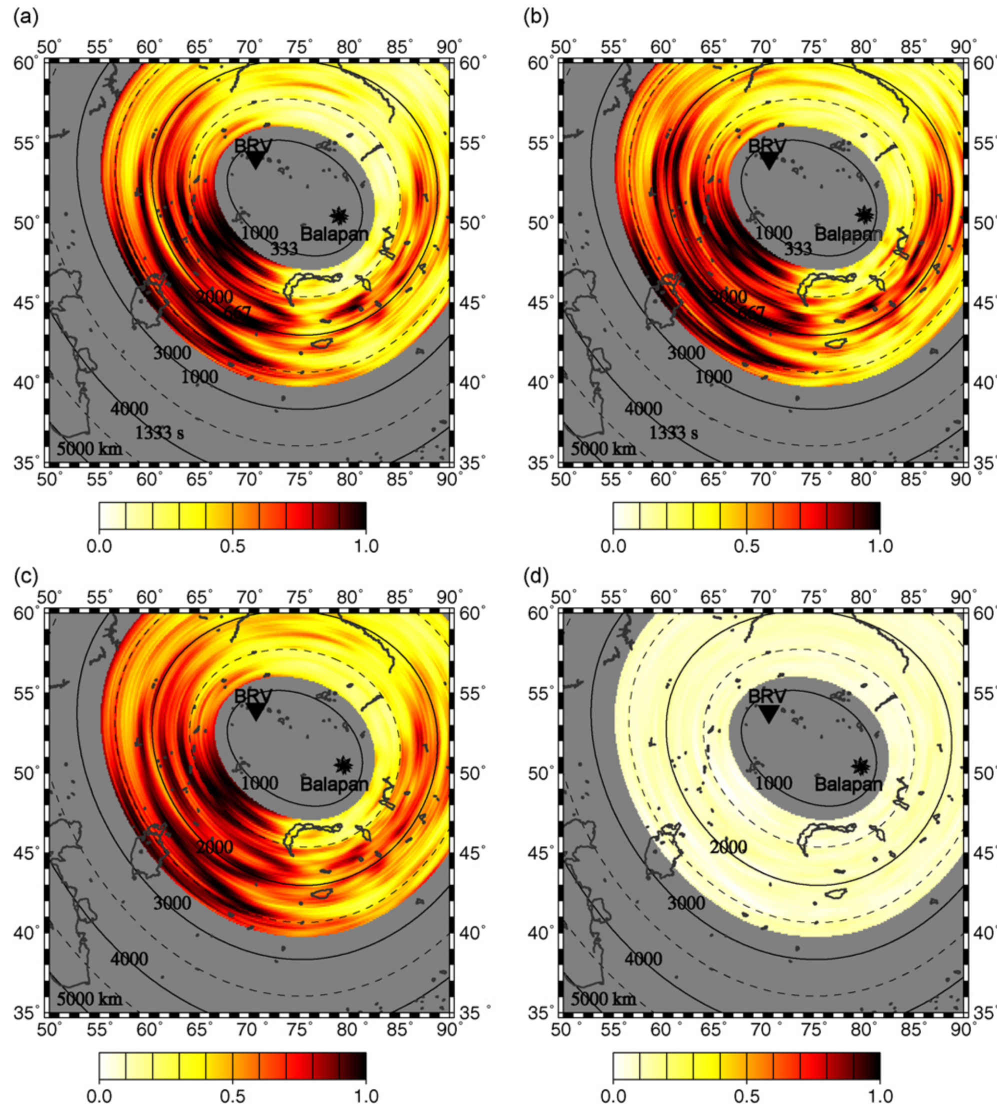

Fig. 13. Bootstrap analysis of Rg scattering intensity: (a) the Rg scattering intensity from the original full data set, (b) an estimate of Rg scattering intensity for a bootstrap set, (c) the average of the results from the 32 bootstrap sets, and (d) the standard deviation among the 32 estimates. Each bootstrap set produces a consistent result that is very close to the result from the original full data set. The average among the 32 results also displays the consistent form. The standard deviations are determined low over the region.

The temporal surplus or shortage of energy from the reference level can be quantified from a relationship between Eqs. (16) and (17):

$$\frac{Q}{Q_{\mathrm{ref}}} = \frac{\Delta E_{\mathrm{ref}}}{\Delta E}. \tag{18}$$

The scattered energy is proportional to the amplitude-square of scattered wave. Thus, the temporal variation of quality factor, $Q(\theta, t)$, can be estimated by

$$Q(\theta, t) = Q_{\mathrm{ref}} \left[\frac{w_{\mathrm{ref}}^{\theta}(t)}{w_{\mathrm{s}}^{\theta}(t)} \right], \tag{19}$$

where Q_{ref} is the reference Q, and $w_{\mathrm{ref}}^{\theta}(t)$ is the reference level of coda.

It is known that the envelope of entire coda is not well represented with a single representative curve due to temporal variations in-phase composition of coda (e.g., Jemberie and Langston, 2005). Thus, we divide the coda sections into several segments, and determine the reference coda envelope separately. We divide the coda sections by 310–340 s, 340–400 s and 400–900 s for analyses of Rg scattered waves, by 270–300 s, 300–340 s, 340–400 s and 400–900 s for analyses of Lg scattered waves, and by 210–240 s, 240–280 s, 280–330 s, 330–400 s and 400–900 s for analyses of Sn scattered waves.

The Q estimates are presented in Fig. 14. The Q estimates agree with previous results (e.g., Jin and Aki, 1988). The overall Q values from Rg scattered waves are lower than those from Lg scattered waves. The Q values from Sn scattered waves are greater than those from Rg and Lg scattered waves. The scattering strength is observed to be different by phase due to dif-

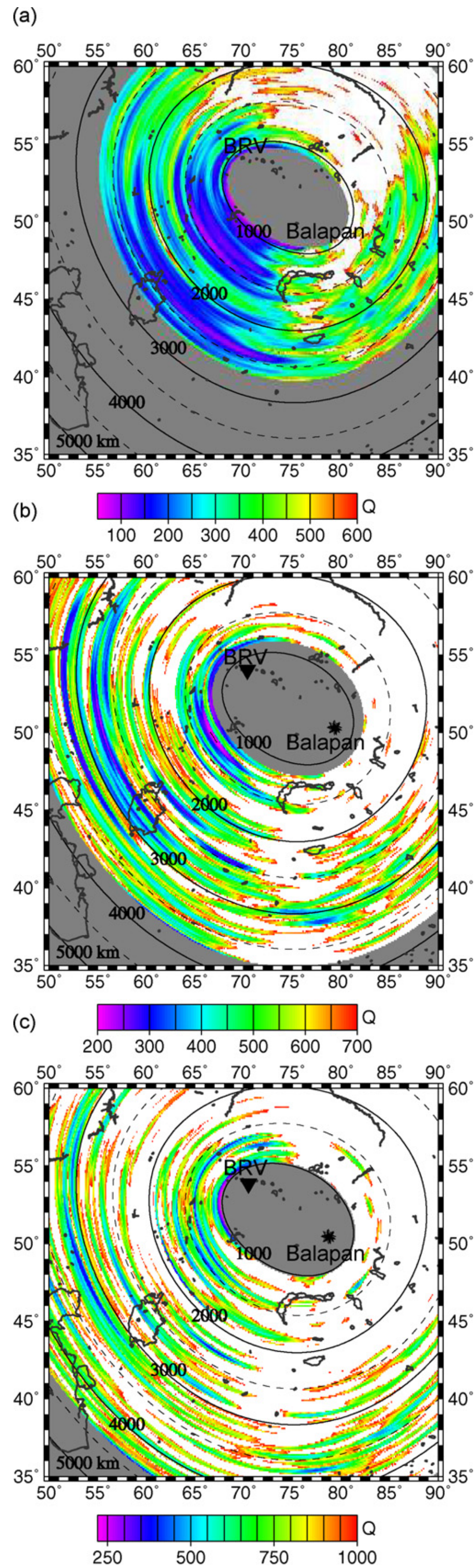

Fig. 14. Spatial variation of quality factors, Q, estimated from (a) Rg, (b) Lg and (c) Sn scattered waves. The quality factors from Rg scattered waves are smaller than those from Lg and Sn scattered waves, which implies a stronger scattering at Rg phase. Rg phase is particularly sensitive to the surface topography compared to Lg and Sn phases. Lg phase is sensitive to most crustal variations. Sn phase is sensitive to the structural variations near the Moho (e.g., thick sedimentary layer, crustal thickness).

ference in ray paths and frequency contents (e.g., Zhang and Lay, 1994).

The mean Q value from Rg scattered-wave analysis, Q_{Rg}, is estimated by ∼400. The presence of sedimentary basin and crustal thinning, causing a blockage of lateral waveguide, appears to play a role as a major source of significant Rg scattering. The Q_{Rg} is estimated by ∼100 for a crustal thinning of 10 km, and ∼250 for a sedimentary thickening of 4 km. The influence of surface topography on Rg scattering is weak compared to the sedimentary layer and crustal thickness. The Q_{Rg} is estimated by ∼350 for a surface-topography change of 2 km.

The illuminated locations of scatterers for Rg scattered energy is similar to those for Lg scattered energy. However, the Q_{Lg} is observed to be greater than Q_{Rg}. The Q_{Lg} is estimated by ∼320 for a 10-km crustal thinning, ∼420 for a 10-km crustal thickening, and ∼500 for 4-km sedimentary thickening. The influence of surface topography is reduced in Lg scattering, and Q_{Lg} is given by ∼550 for a 2-km surface relief. The Sn phase is sensitive to structural variations at the lower crust and upper mantle, which may be primarily sensitive to the Moho topography and thick sedimentary layer. The quality factor, Q_{Sn}, is estimated by ∼400 for a 10-km crustal thinning, and ∼650 for 4-km sedimentary thickening.

8. Discussion and conclusions

We have devised a technique to image laterally varying regional heterogeneities from seismic coda of source-array records. Coherent scattered energy in the source-array coda is extracted from the source-array coda, and is quantified in terms of scattering intensity and quality factor. The estimated quality factors are apparent scattering Q that accounts for scattering Q on the ray paths. The scattering intensity and quality factors illuminate regional structural variations that are associated with crustal thickening/thinning, sedimentary blockage and surface topography. The influence of geological structures on the scattering magnitude varies with the phase velocity and the frequency of wave. The high correlations between the scattering intensity and geological structures support that the proposed methodology is sufficient for imaging of scatterers in far-regional distances.

The proposed technique shows promises for the study of laterally varying geological and tectonic structures in a region with poor coverage of seismic monitoring (e.g., low great-circle path coverage, limited number of available stations). Such regions include subduction zones and mid-ocean ridges, which naturally accompany clustered events. The technique is able to detect topographic variation of internal boundaries within the crust and lithosphere. The technique may be extended for sounding of intrusive or high-impedance materials, such as magma chamber and partial melting material in the medium (Tusa et al., 2004).

In the source-array analysis, however, the arc length of isochrone increases with the distance from the source array. This implies that the resolution for far-distance scatterers can be poor in the single-side array analyses, including both source-array and receiver-array analyses, due to smearing of scattering intensity along isochronic arc. The double-beamforming technique utilizing both source and receiver arrays may be an alternative way to overcome such limitation of single-side array techniques. The double-beamforming technique, in principle, allows precise positioning of scatterer at far distance. The double-beamforming technique has already been found useful for imaging heterogeneities in the Earth's deep interior (Scherbaum et al., 1997; Krüger et al., 2001; Lay et al., 2004).

Unwanted multiple scattered waves, however, still exist in the double-beamformed records, which causes uncertainty in positioning of long-distance scatterers. Further, cases where both source and receiver array are available are very rare in the nature, which enforces us to use single-side array data. An alternative way, which may be more practical, is to analyze a set of of single-side array system. The set of single-side arrays can be composed of several source and/or receiver arrays. Stacking of results from the single-side arrays may help to increase the resolution of imaging. Also, it appears that refinement of hypocenters and origin times may be needed for accurate and stable analysis in the application to natural earthquake data using a relocation scheme (VanDecar and Crosson, 1990; Waldhauser and Ellsworth, 2000).

Acknowledgements

We thank Jiakang Xie for valuable discussions on source-array data. We are grateful to Won-Young Kim and Vitaly Khalturin for information on the Balapan explosion records. We thank Professors George Helffrich and Thorne Lay, and an anonymous reviewer for constructive comments. WM was partially supported by the US Department of Energy under contract DE-FC52-03NA99514. TKH was supported by the Korea Meteorological Administration Research and Development Program under Grant CATER 2007-5111.

Appendix A. Ensemble-averaged amplitude squares in random media

Regional phases exhibit a strong impetus of lateral propagation in the crust and lithosphere. The scattering of such regional phases can be well represented with a 2D model (Jemberie and Langston, 2005). The ensemble-averaged amplitude squares in 2D random media for P-wave incidence are given by (Hong and Kennett, 2003),

$$\begin{aligned}
\langle |u^{\mathrm{PP}}|^2 \rangle &= \frac{k_\alpha^3 \mathsf{S}}{8\pi l} [C^{\mathrm{PP}}(\phi)]^2 \, \mathcal{P}\left[2k_\alpha \sin\frac{\phi}{2}\right], \\
\langle |u^{\mathrm{PS}}|^2 \rangle &= \frac{k_\alpha^3 \gamma^3 \mathsf{S}}{8\pi l} [C^{\mathrm{PS}}(\phi)]^2 \, \mathcal{P}\left[k_\alpha \sqrt{1+\gamma^2-2\gamma\cos\phi}\right].
\end{aligned} \tag{A.1}$$

and for S-wave incidence (Hong, 2004),

$$\begin{aligned}
\langle |u^{\mathrm{SP}}|^2 \rangle &= \frac{k_\alpha^3 \mathsf{S}}{\gamma^2 8\pi l} [C^{\mathrm{SP}}(\phi)]^2 \, \mathcal{P}\left[k_\alpha \sqrt{1+\gamma^2-2\gamma\cos\phi}\right], \\
\langle |u^{\mathrm{SS}}|^2 \rangle &= \frac{k_\beta^3 \mathsf{S}}{8\pi l} [C^{\mathrm{SS}}(\phi)]^2 \, \mathcal{P}\left[2k_\beta \sin\frac{\phi}{2}\right],
\end{aligned} \tag{A.2}$$

where k_α and k_β are the wavenumbers of P- and S-waves, γ is the ratio of background P- and S-wave velocities (α_0/β_0), S is the surface area of heterogeneity, l is the propagation distance, ϕ is the scattering angle, and $\mathcal{P}$ is the spectral density function of the random medium. The coefficient C^{ij} ($i, j = \mathrm{P}, \mathrm{S}$) is given by

$$\begin{aligned}
C^{\mathrm{PP}}(\phi) &= \sin\phi \left\{C_1^{\mathrm{P}} A_{11}^{\mathrm{P}}(\phi)\sin\phi + 2A_{12}^{\mathrm{P}}(\phi) + C_2^{\mathrm{P}} A_{12}^{\mathrm{P}}(\phi)(\cos\phi - 1)\right\} + \cos\phi\{C_1^{\mathrm{P}} A_{21}^{\mathrm{P}}(\phi)\sin\phi + 2A_{22}^{\mathrm{P}}(\phi) + C_2^{\mathrm{P}} A_{22}^{\mathrm{P}}(\phi)(\cos\phi - 1)\}, \\
C^{\mathrm{PS}}(\phi) &= \cos\phi\{C_1^{\mathrm{P}} A_{11}^{\mathrm{S}}(\phi)\gamma\sin\phi + 2A_{12}^{\mathrm{S}}(\phi) + C_2^{\mathrm{P}} A_{12}^{\mathrm{S}}(\phi)(\gamma\cos\phi - 1)\} - \sin\phi\{C_1^{\mathrm{P}} A_{21}^{\mathrm{S}}(\phi)\gamma\sin\phi + 2A_{22}^{\mathrm{S}}(\phi) + C_2^{\mathrm{P}} A_{22}^{\mathrm{S}}(\phi)(\gamma\cos\phi - 1)\}, \\
C^{\mathrm{SP}}(\phi) &= \sin\phi\{-\gamma C_1^{\mathrm{S}} A_{11}^{\mathrm{P}}(\phi) + (\cos\phi - \gamma)C_2^{\mathrm{S}} A_{11}^{\mathrm{P}}(\phi) + \sin\phi\, C_2^{\mathrm{S}} A_{12}^{\mathrm{P}}(\phi)\} + \cos\phi\{-\gamma C_1^{\mathrm{S}} A_{21}^{\mathrm{P}}(\phi) + (\cos\phi - \gamma)C_2^{\mathrm{S}} A_{21}^{\mathrm{P}}(\phi) + \sin\phi\, C_2^{\mathrm{S}} A_{22}^{\mathrm{P}}(\phi)\}, \\
C^{\mathrm{SS}}(\phi) &= \cos\phi\{-C_1^{\mathrm{S}} A_{11}^{\mathrm{S}}(\phi) + (\cos\phi - 1)C_2^{\mathrm{S}} A_{11}^{\mathrm{S}}(\phi) + \sin\phi\, C_2^{\mathrm{S}} A_{12}^{\mathrm{S}}(\phi)\} - \sin\phi\{-C_1^{\mathrm{S}} A_{21}^{\mathrm{S}}(\phi) + (\cos\phi - 1)C_2^{\mathrm{S}} A_{21}^{\mathrm{S}}(\phi) + \sin\phi\, C_2^{\mathrm{S}} A_{22}^{\mathrm{S}}(\phi)\},
\end{aligned} \tag{A.3}$$

where C_i^j ($i = 1, 2$, $j = \mathrm{P}, \mathrm{S}$) is

$$\begin{aligned}
C_1^{\mathrm{P}} &= (K+2)\left(1 - \frac{2}{\gamma^2}\right), \qquad C_2^{\mathrm{P}} = K+2, \\
C_1^{\mathrm{S}} &= -2, \qquad C_2^{\mathrm{S}} = K+2,
\end{aligned} \tag{A.4}$$

and K is the constant in (1). Also, A_{ij}^k ($i, j = 1, 2$, $k = \mathrm{P}, \mathrm{S}$) is given by

$$\begin{aligned}
A_{11}^{\mathrm{P}}(\phi) &= \sin^2\phi, \qquad A_{12}^{\mathrm{P}}(\phi) = \sin\phi\cos\phi, \\
A_{21}^{\mathrm{P}}(\phi) &= -\sin\phi\cos\phi, \qquad A_{22}^{\mathrm{P}}(\phi) = \cos^2\phi, \\
A_{11}^{\mathrm{S}}(\phi) &= \cos^2\phi, \qquad A_{12}^{\mathrm{S}}(\phi) = -\sin\phi\cos\phi, \\
A_{21}^{\mathrm{S}}(\phi) &= \sin\phi\cos\phi, \qquad A_{22}^{\mathrm{S}}(\phi) = \sin^2\phi.
\end{aligned} \tag{A.5}$$

References

Aki, K., 1980. Attenuation of shear-waves in the lithosphere for frequencies from 0.005 to 25 Hz. Phys. Earth Planet. Inter. 21, 50–60.

Aki, K., Chouet, B., 1975. Origin of coda waves: source, attenuation, and scattering effects. J. Geophys. Res. 80, 3322–3342.

Aki, K., Richards, P.G., 1980. Quantitative Seismology, Theory and Methods, vol. II. W.H. Freeman and Company, San Francisco.

Bassin, C., Laske, G., Masters, G., 2000. The current limits of resolution for surface wave tomography in North America. EOS Trans. AGU 81, F897.

Birch, F., 1960. The velocity of compressional waves in rocks to 10 kilobars, part 1. J. Geophys. Res. 65, 1083–1102.

Bostock, M.G., 1991. Surface wave scattering from 3-D obstacles. Geophys. J. Int. 104, 351–370.

Boucher, G., 1973. Local seismic phenomena in the first three seconds after underground nuclear explosions. J. Geophys. Res. 78, 1348–1360.

Chen, X., Long, L.T., 2000. Spatial distribution of relative scattering coefficients determined from microearthquake coda. Bull. Seism. Soc. Am. 90 (2), 512–524.

Dainty, A.M., Schultz, C.A., 1995. Crustal reflections and the nature of regional *P* coda. Bull. Seism. Soc. Am. 85, 851–858.

Efron, B., Tibshirani, R., 1991. Statistical data analysis in the computer age. Science 253, 390–395.

Fehler, M., Hoshiba, M., Sato, H., Obara, K., 1992. Separation of scattering and intrinsic attenuation for the Kanto-Tokai region, Japan, using measurements of S-wave energy versus hypocentral distance. Geophys. J. Int. 108, 787–800.

Frankel, A., Clayton, R.W., 1986. Finite difference simulations of seismic scattering: implications for the propagation of short-period seismic waves in the crust and models of crustal heterogeneity. J. Geophys. Res. 91, 6465–6489.

Gupta, I.N., Lynnes, C.S., McElfresh, T.W., Wagner, R.A., 1990. F-K analysis of Noress array and single station data to indentify sources of near-receiver and near-source scattering. Bull. Seism. Soc. Am. 80, 2227–2241.

Hedlin, M.A.H., Shearer, P.M., Earle, P.S., 1997. Seismic evidence for small-scale heterogeneity throughout the Earth's mantle. Nature 387, 145–150.

Hong, T.-K., 2004. Scattering attenuation ratios of *P* and *S* waves in elastic media. Geophys. J. Int. 158, 211–224.

Hong, T.-K., Kennett, B.L.N., 2003. Scattering attenuation of 2-D elastic waves: theory and numerical modelling using a wavelet-based method. Bull. Seism. Soc. Am. 93, 922–938.

Hong, T.-K., Menke, W., 2008. Constituent energy of regional seismic coda, Bull. Seism. Soc. Am., in press.

Hong, T.-K., Wu, R.-S., Kennett, B.L.N., 2005. Stochastic features of scattering. Phys. Earth Planet. Inter. 148, 131–148.

Hong, T.-K., Xie, J., 2005. Phase composition of regional seismic waves from underground nuclear explosions. J. Geophys. Res. 110, B12302, doi:10.1029/2005JB003753.

Hoshiba, M., Rietbrock, A., Scherbaum, F., Nakahara, H., Haberland, C., 2001. Scattering attenuation and intrinsic absorption using uniform and depth dependent model - Application to full seismogram envelope recorded in Northern Chile. J. Seism. 5, 157–179.

Jemberie, A.L., Langston, C.A., 2005. Site amplification, scattering, and intrinsic attenuation in the Mississippi embayment from coda waves. Bull. Seism. Soc. Am. 95, 1716–1730.

Jin, A., Aki, K., 1988. Spatial and temporal correlation between coda Q and seismicity in China. Bull. Seism. Soc. Am. 78, 741–769.

Kanasewich, E.R., 1981. Time Sequence Analysis in Geophysics, third ed. The University of Alberta Press, Alberta, Canada.

Kennett, B.L.N., 2002. The Seismic Wavefield, Volume II, Interpretation of Seismograms on Regional and Global Scales. Cambridge University Press, New York.

Kennett, B.L.N., Furumura, T., 2001. Regional phases in continental and oceanic environments. Geophys. J. Int. 146, 562–568.

Kim, W.-Y., Richards, P.G., Adushkin, V., Ovtchinnikov, V., 2001. Borovoye digital seismogram archive for underground nuclear tests during 1966-1996, Technical Report, Lamont-Doherty Earth Observatory of Columbia University.

Krüger, F., Baumann, M., Scherbaum, F., Weber, M., 2001. Mid mantle scatterers near the Mariana slab detected with a double array method. Geophys. Res. Lett. 28, 667–670.

Laske, G., Masters, G., 1997. A global digital map of sediment thickness. EOS Trans. AGU 78, 483.

Lay, T., 1987. Analysis of near-source contributions to early P-wave coda for underground explosions. III. Inversion for isotropic scatterers. Bull. Seism. Soc. Am. 77, 1767–1783.

Lay, T., Garnero, E.J., Russell, S.A., 2004. Lateral variation of the D" discontinuity beneath the Cocos Plate. Geophys. Res. Lett. 31, L15612, doi:10.1029/2004GL020300.

La Rocca, M., Del Pezzo, E., Simini, M., Scarpa, R., De Luca, G., 2001. Array analysis of seismograms from explosive sources: Evidence for surface waves scattered at the main topographical features. Bull. Seism. Soc. Am. 91, 219–231.

Levashova, N.M., Degtyarev, K.E., Bazhenov, M.L., Collins, A.Q., van der Voo, R., 2003. Permian palaeomagnetism of East Kazakstan and the amalgamation of Eurasia. Geophys. J. Int. 152, 677–687.

Lynnes, C.S., Lay, T., 1989. Inversion of P coda for isotropic scatterers at the Yucca Flat test site. Bull. Seism. Soc. Am. 79, 790–804.

Matsumoto, S., Obara, K., Hasegawa, A., 1998. Imaging P-wave scatterer distribution in the focal area of the 1995 M7.2 Hyogo-ken Nanbu (Kobe) earthquake. Geophys. Res. Lett. 25, 1439–1442.

Matsumoto, S., Obara, K., Hasegawa, A., 2001. Characteristics of coda envelope for slant-stacked seismogram. Geophys. Res. Lett. 28, 1111–1114.

Mitchell, B.J., 1981. Regional variation and frequency dependence of Q_β in the crust of the United States. Bull. Seism. Soc. Am. 71, 1531–1538.

Nikolaev, A.V., Troitskiy, P.A., 1987. Lithospheric studies based on array analysis of P-coda and microseismics. Tectonophysics 140, 103–113.

NNCRK, 1999. Technical Report, Proceedings of the Workshop on IMS Location Calibration, contributed by the National Nuclear Centre of the Republic of Kazakhstan, Olso, January 1999.

Quin, H.R., Thurber, C.H., 1992. Seismic velocity structure and event relocation in Kazakhstan from secondary *P* phases. Bull. Seism. Soc. Am. 82, 2494–2510.

Revenaugh, J., 1995. A scattered-wave image of subduction beneath the transverse range. Science 268, 1888–1892.

Revenaugh, J., Meyer, R., 1997. Seismic evidence of partial melt within a possibly ubiquitous low-velocity layer at the base of the mantle. Science 277, 670–673.

Rost, S., Thomas, C., 2002. Array seismology: methods and applications. Rev. Geophys. 40 (3), 1008, doi:10.1029/2000RG000100.

Sato, H., Fehler, M., 1998. Wave Propagation and Scattering in the Heterogeneous Earth. Springer-Verlag, New York.

Sato, H., Nishino, M., 2002. Multiple isotropic-scattering model on the spherical Earth for the synthesis of Rayleigh-wave envelopes. J. Geophys. Res. 107 (B12), 2343, doi:10.1029/2001JB000915.

Scherbaum, F., Gillard, D., Deichmann, N., 1991. Slowness power spectrum analysis of the coda composition of two microearthquake clusters in northern Switzerland. Phys. Earth Planet. Inter. 67, 137–161.

Scherbaum, F., Krüger, F., Weber, M., 1997. Double beam imaging: Mapping lower mantle heterogeneities using combinations of source and receiver arrays. J. Geophys. Res. 102, 507–522.

Shapiro, N.M., Campillo, M., Margerin, L., Singh, S.K., Kostoglodov, V., Pacheco, J., 2000. The energy partitioning and the diffusive character of the seismic coda. Bull. Seism. Soc. Am. 90, 655–665.

Shiomi, K., Sato, H., Ohtake, M., 1997. Broadband power-law spectra of well-log data in Japan. Geophys. J. Int. 130, 57–64.

Snieder, R., 1986. The influence of topography on the propagation and scattering of surface waves. Phys. Earth Planet. Inter. 44, 226–241.

Snieder, R., 1988. Large-scale waveform inversions of surface waves for lateral heterogeneity, 1. Theory and numerical examples. J. Geophys. Res. 93, 12055–12065.

Spudich, P., Bostwick, T., 1987. Studies of the seismic coda using an earthquake cluster as a deeply buried seismograph array. J. Geophys. Res. 92, 10526–10546.

Stewart, R., Peselnick, L., 1977. Velocity of compressional waves in dry Franciscan rocks to 8 kbar and 300°C. J. Geophys. Res. 82, 2027–2039.

Thurber, C., Trabant, C., Haslinger, F., Hartog, R., 2001. Nuclear explosion locations at the Balapan, Kazakhstan, nuclear test site: the effects of high-precision arrival times and three-dimensional structure. Phys. Earth Planet. Inter. 123, 283–301.

Toksöz, M.N., Dainty, A.M., Reiter, E.R., Wu, R.S., 1988. A model for attenuation and scattering in the earth's crust. Pure Appl. Geophys. 128, 81–100.

Tusa, G., Malone, S.D., Giampiccolo, E., Gresta, S., Musumeci, C., 2004. Attenuation of Short-Period P Waves at Mount St. Helens. Bull. Seism. Soc. Am. 94, 1441–1455.

VanDecar, J.C., Crosson, R.S., 1990. Determination of teleseismic relative phase arrival times using multi-channel cross correlation and least squares. Bull. Seism. Soc. Am. 80, 150–169.

Vidale, J.E., Hedlin, M.A.H., 1998. Evidence for partial melt at the core-mantle boundary north of Tonga from the strong scattering of seismic waves. Nature 391, 682–685.

Waldhauser, F., Ellsworth, W.L., 2000. A double-difference earthquake location algorithm: method and application to the northern Hayward fault, California. Bull. Seism. Soc. Am. 90, 1353–1368.

Wu, R.S., 1982. Attenuation of short period seismic waves due to scattering. Geophys. Res. Lett. 9, 9–12.

Xie, J., Cong, L., Mitchell, B.J., Chiu, J.M., 1996. Complexities in high-frequency seismic waveforms due to three-dimensional structure in the New Madrid Seismic Zone. J. Geophys. Res. 101, 5751–5778.

Zhang, T., Lay, T., 1994. Analysis of short-period regional phase path effects associated with topography in Eurassia. Bull. Seism. Soc. Am. 84, 119–132.

Zhang, T., Lay, T., 1995. Why the Lg phase does not traverse oceanic crust. Bull. Seism. Soc. Am. 85, 1665–1678.